

A Detailed Modeling Study of Radiative Heat Transfer in a Heavy-Duty Diesel Engine

C. Paul^{a,*}, Sebastian Ferreyro Fernandez^a, D. C. Haworth^a, S. Roy^b, M. F. Modest^c

^a*Department of Mechanical and Nuclear Engineering, The Pennsylvania State University, University Park, PA 16802, USA*

^b*Marquette University, Milwaukee, WI, USA*

^c*University of California, Merced, CA, USA*

Abstract

In recent years, the importance of radiative heat transfer in combustion has been increasingly recognized. Detailed models have become available that accurately represent the complex spectral radiative properties of reacting gas mixtures and soot particles, and new methods have been developed to solve the radiative transfer equation (RTE). At the same time, the trends toward higher operating pressures and higher levels of exhaust-gas recirculation in compression-ignition engines, together with the demand for higher quantitative accuracy from in-cylinder CFD models, has led to renewed interest in radiative transfer in engines. Here an in-depth investigation of radiative heat transfer is performed for a heavy-duty diesel truck engine over a range of operating conditions. Results from 10 different combinations of turbulent combustion models, spectral radiation property models, and RTE solvers are compared to provide insight into the global influences of radiation on energy redistribution in the

*Corresponding author:
Email address: cxp484@psu.edu (C. Paul)

combustion chamber, heat losses, and engine-out pollutant emissions (NO and soot). Also, the relative importance of the individual contributions of molecular gas versus soot radiation, the spectral model, the RTE solver, and unresolved turbulent fluctuations in composition and temperature (turbulence-radiation interactions – TRI) are investigated. Local instantaneous temperatures change by as much as 100 K with consideration of radiation, but the global influences of radiation on heat losses and engine-out emissions are relatively small (in the 5-10% range). Molecular gas radiation dominates over soot radiation, consideration of spectral properties is essential for accurate predictions of reabsorption, a simple RTE solver (a first-order spherical harmonics – P1 – method) is sufficient for the conditions investigated, and TRI effects are small (less than 10%). While the global influences of radiation are relatively small, it is nevertheless desirable to explicitly account for radiation in in-cylinder CFD. To that end, a simplified CFD radiation model has been proposed, based on the findings reported here.

Keywords: Radiative heat transfer, Compression-ignition engine, Spectral radiation modeling, Turbulence-radiation interaction, Stochastic modeling

1. Introduction

Heat losses play a significant role in determining engine efficiency, and reducing in-cylinder heat losses has been a primary focus in developing advanced engine combustion systems. In-cylinder heat losses usually are dominated by turbulent boundary layer convective heat losses at walls, and most engine heat transfer experimental and modeling studies have focused on convective heat transfer. Radiation can contribute significantly to heat losses in very large bore,

heavy-duty diesel engines [1], but conventional wisdom has been that in-cylinder radiation was dominated by soot, and that radiation was of secondary importance in car and truck engines.

Few in-cylinder CFD modeling studies have considered radiation heat transfer, and only a subset of those has considered a radiatively participating medium by solving a radiative transfer equation (RTE) [2–5]. Mengüç et al. [2] solved the RTE using first- and third- order spherical harmonics approximations (P_1 and P_3) with emphasis on scattering by fuel droplets. They concluded that, even though P_3 provides better accuracy than P_1 , a P_1 -approximation in diesel engine simulations seems acceptable, and scattering by fuel droplets can be neglected. Abraham and Magi [3] used a discrete ordinate method (DOM) as a RTE solver to compute radiative heat loss in a diesel engine and concluded that with consideration of radiative heat loss, NO_x concentration is lowered, but the soot concentrations are not altered significantly. Wiedenhoefer and Reitz [4] developed a radiation model using a DOM RTE solver and the wide-band spectral model of Siegel and Howell [6] to obtain gas and soot absorption coefficients. They have shown that the low-order DOM approximation (S_2) gives sufficient accuracy for the radiation heat flux provided that the local extinction coefficient is large, as is the case with even small quantities of soot. Yoshikawa and Reitz [5] investigated the effect of radiation on NO_x and soot emission using a DOM RTE solver along with a gray gas assumption and Yuen and Tien's [7] soot emissivity calculation. They concluded that the effect of radiation on NO_x and soot emission is small, but the influence of radiation was larger on soot formation than NO_x formation. However, to date, none of the studies have yet used detailed radiation models such as a photon Monte Carlo (PMC) RTE

solver along with a line-by-line (LBL) spectral model for engine radiative heat transfer analysis.

In the meantime, next-generation high-efficiency engines are expected to function closer to the limits of stable operation, where even small variations in the in-cylinder thermochemical environment may manifest globally in reduced efficiency and/or increased pollutant emissions. Current trends include higher operating pressures and higher levels of exhaust-gas recirculation (EGR), both of which will enhance molecular gas radiation. At the same time, increasing accuracy is being demanded from CFD models for in-cylinder processes, including quantitatively accurate predictions of efficiency and pollutant emissions. In recent years, sophisticated radiation models that account accurately for the spectral properties of the reacting mixture have become available, and these are being applied with increasing frequency in CFD modeling studies of luminous and nonluminous laboratory flames [8–12]. Recently, detailed investigations of radiative heat transfer under engine-relevant conditions using high-fidelity spectral models have been reported by Fernandez et al. [11] for the Engine Combustion Network “Spray A” flame: a high-pressure turbulent spray flame using n-dodecane fuel. This study included investigations of the influence of unresolved turbulent fluctuations in composition and temperature on radiative emission and reabsorption (turbulence-radiation interactions – TRI), which were found to be relatively small (approximately 10%). In another study of the “Spray A” flame, Bolla et al. [12] used DOM with a gray-gas spectral model. They used the optically thin fluctuation approximation [13] to capture emission TRI effects, while absorption TRI is neglected. They also reported that the influence of unresolved turbulent fluctuations on radiative emission and

reabsorption is small (~10%).

In this paper, an in-depth investigation of in-cylinder radiative heat transfer is reported for a heavy-duty diesel truck engine over a range of operating conditions. Multiple spectral radiation models and RTE solvers have been implemented to perform coupled simulations, where the radiative source term feeds back to the CFD through the enthalpy equation. The results provide new insight into the radiative environment in engines and other high-pressure turbulent combustion systems, including the influence of radiation on energy redistribution in the combustion chamber, heat losses, and pollutant emissions. The relative importance of various aspects of the problem is elucidated, including molecular gas radiation versus soot radiation, spectral properties of the reacting mixture, the method used to compute the local radiative intensity (RTE solver), and turbulence-radiation interactions. Based on these findings, a simplified CFD model for in-cylinder radiative transfer has been proposed and demonstrated in a separate publication [14].

2. Engine configuration and operating conditions

A detailed investigation of in-cylinder radiative heat transfer is performed for a Volvo 13L production six-cylinder heavy-duty diesel truck engine. This is the same engine that was the subject of an earlier modeling study [15] that focused on the influence of unresolved turbulent fluctuations in composition and temperature on combustion chemistry and pollutant emissions (turbulence-chemistry interactions – TCI). Key geometric parameters are a bore, stroke and compression ratio of 13.1 cm, 15.8 cm and 15.8:1, respectively. The engine speed is 1,213 r/min, and the initial (post-intake-valve-closure) in-cylinder swirl

Table 1: Initial conditions and fuel-injection parameters for four engine operating conditions.

	EGR		Synthetic EGR	
	Part-load	Full-load	Part-load	Full-load
Initial conditions:				
Pressure (bar)	5.65	14.28	5.65	14.28
Temperature (K)	540.9	560.9	540.9	560.9
Initial composition (% mass)	O ₂	18.68	18.84	18.68
	N ₂	75.72	75.75	81.32
	H ₂ O	4.06	3.92	0.0
	CO ₂	1.54	1.49	0.0
Fuel-injection parameters:				
Start of injection (bTDC)	2.8°	4.6°	2.8°	4.6°
End of injection (aTDC)	3.5°	16.8°	3.5°	16.8°
Fuel mass injected for 1/6 sector (mg)	13	47	13	47

ratio is 0.3. Experimental data are available for full-load and part-load operating conditions, each with two different levels of EGR (Table 1). For present purposes, EGR is modeled by appropriate initial mass fractions of CO₂ and H₂O. For the “synthetic EGR” cases, the O₂ mass fraction is kept the same as for the corresponding EGR case, and the rest of the in-cylinder mixture is prescribed simply as N₂. These “synthetic EGR” cases are used to determine whether or not the EGR has a significant influence on radiation for the same fuel-oxygen ratio.

3. Physical Models and Numerical Methods

An unsteady Reynolds-averaged Navier-Stokes (URANS) formulation is adopted, using solvers based on the OpenFOAM v2.3.x toolbox [16]. A sector mesh centered on one of the six spray plumes is used, with cyclic symmetry conditions on the lateral faces. Constant wall temperatures of 553 K and 535 K are used for full-load and part-load operating conditions, respectively. Simulations begin after intake-valve closure at 60° before piston top-dead-center (bTDC), and continue until 120° after top-dead-center (aTDC), before exhaust-valve opening. A deforming grid is used to accommodate the moving piston. To maintain acceptable mesh quality throughout the simulation, two meshes of 51,225 and 85,650 cells (Fig. 1) are used. The former mesh is used between 30° bTDC and 30° aTDC, and the latter mesh is used for the remainder of the simulation. Field variables are mapped between the meshes using a conservative volume-weighted mapping scheme. A computational time step of $3.4\ \mu\text{s}$ (0.025 crank-angle-degrees of rotation – CAD) is used, in all cases.

Physical models and numerical methods for processes other than radiative heat transfer are introduced in the first subsection below. This is followed by a description of the radiation models. In the final subsection, the model combinations for which results will be presented are summarized.

3.1. *Physical processes other than radiation*

The mean continuity, momentum and pressure equations for a chemically reacting ideal-gas mixture are solved using a finite-volume method with second-order spatial discretizations and first-order implicit time discretization, and a standard two-equation $k - \epsilon$ turbulence model [17] with wall functions. Values

of model constants are given in Table 2. For wall heat transfer, Angelberger's wall-function model [18] is used, which takes into account the variations of viscosity and density with temperature in the boundary layer. Relatively fine extruded meshes (five layers in 0.5 mm) are used adjacent to the walls (cylinder-head, piston, and liner).

A 42-species chemical mechanism (40-species n-heptane [19], plus two additional species for thermal NO) is used to represent the gas-phase chemistry, and a semi-empirical two-equation model is used for soot [20]. For soot, two additional modeled "species" equations are solved for soot mass fraction and particle number density. The soot model includes representations for particle inception, surface growth, oxidation, and coagulation. Inception is based on acetylene (C_2H_2). Soot oxidation pathways were augmented to consider oxidation by OH and O (in addition to O_2), with the addition of the two reactions suggested in [21]. The soot surface growth rate was tuned to give reasonable agreement with measured engine-out soot levels for the four operating conditions.

One of two approaches is used for turbulent combustion modeling: a locally well-stirred reactor (WSR) model, or a transported composition probability density function (tPDF) model. For the WSR model, mean species mass fraction and mixture specific enthalpy equations are solved using the finite-volume method, and mean chemical source terms are computed using finite-volume cell-mean compositions and temperatures; this model neglects the influence of turbulent fluctuations in composition and temperature on mean density and reaction rates (no TCI). For the tPDF model, species mass fraction and mixture specific enthalpy equations are solved using a notional stochastic

Lagrangian particle method that explicitly accounts for turbulent fluctuations in composition and temperature (TCI) [22, 23]; the number of notional particles per finite-volume cell is controlled to remain between 50 and 100. In both the WSR and tPDF models, turbulent fluxes of species and enthalpy are modeled using a gradient transport assumption with unity turbulent Schmidt and Prandtl numbers. In the tPDF model, molecular transport (“mixing”) of species and enthalpy is modeled using the Euclidean minimum spanning tree (EMST) model [24], with a constant value of the model coefficient C_ϕ ($C_\phi=5.0$).

Liquid fuel injection and spray evolution are modeled using a conventional stochastic Lagrangian parcel method [25]. The spray is represented by a finite number of parcels, where each parcel represents a group of droplets having the same properties. To represent spray atomization near the nozzle, a simple blob model [26] is employed. In this model the parcels are injected with a Rosin-Rammler size distribution [27] for droplet diameter. For secondary breakup, the Reitz-Diwakar model [28, 29] is used. These models are not considered to be truly predictive; rather, the models are tuned to give reasonable liquid penetration rates under engine-relevant conditions [11]. Values of the spray model constants are summarized in Table 2. In the tPDF model, the coupling between Lagrangian spray parcels and notional PDF particles is accomplished by distributing the mass and enthalpy of each cell’s vaporizing fuel over the gas-phase notional particles in the cell, in proportion to each notional particle’s mass. The model parameters have been calibrated to match the experimental pressure and heat-release-rate traces using the tPDF model, and then the same parameter values are used for the WSR model.

Table 2: Summary of turbulence and spray model constants.

<i>k</i> – ϵ model constants:	
$C_{\mu}=0.09$ (multiplies k^2/ϵ to give the apparent turbulent viscosity)	
$C_{\epsilon 1}=1.50, C_{\epsilon 2}=1.92, C_{\epsilon 3}=-0.33$ (coefficients in the modeled ϵ equation)	
$\sigma_k=1.00, \sigma_{\epsilon}=1.39$ (turbulent Schmidt numbers in the k and ϵ equations, respectively)	
Spray model constants:	
Atomization (Rosin-Rammler distribution)	Nozzle diameter, $D_N=0.21$ mm Min. droplet diameter, $D_{min}=10^{-3}$ mm Max. droplet diameter, $D_{max}=0.21$ mm Sauter mean diameter, $D_s=0.1$ mm Distribution exponent, $q=3.5$
Secondary breakup (Reitz-Diwakar model)	LBU = 0.75 (normalized distance from nozzle at which secondary breakup is enabled) $C_{bag} = 6.0$ (critical Weber number for bag-type breakup) $C_b = 3.14$ (time factor for bag-type breakup) $C_{strip} = 0.5$ (Weber number factor for stripping-type breakup) $C_s = 19$ (time factor for stripping-type breakup)

3.2. Radiation modeling

A review of the theory and applications of radiative heat transfer in turbulent combustion systems can be found in [30]. In hydrocarbon-fueled engines, the principal participating molecular gases are CO_2 , H_2O , and CO , along with soot particles.

Molecular gases emit and absorb in discrete wavenumber bands. Here the spectral radiative properties of CO_2 , H_2O , and CO are obtained from the HITEMP2010 [31] database; those are tabulated for pressures from 0.1 bar to 80 bar, temperatures from 300 K to 3000 K, and for various mole fractions of the participating species. Simple pressure-based scaling is used to extrapolate to higher pressures. The broadband spectral absorption coefficient for soot is evaluated using the small-particle limit (Rayleigh theory) [32] with the spectral variation of

the complex index of refraction taken from [33]; scattering is neglected. Spray radiation is negligible for the conditions that are of interest here [30]. From the spectral molecular-gas databases and the presumed soot radiative properties, a hierarchy of spectral models is constructed. These range from full line-by-line (LBL), to high-fidelity full-spectrum k -distributions (FSK), to gray-gas models with Planck-mean absorption coefficients [32]. For present purposes, the combustion chamber walls are taken to be cold and black.

Multiple radiative transfer equation (RTE) solvers have been implemented to calculate the local radiative intensity in situations where reabsorption is considered. These include the stochastic photon Monte Carlo (PMC) method where no intrinsic assumptions are invoked regarding the directional distribution of radiative intensity, spherical-harmonics methods (SHM), and discrete-ordinates methods (DOM) [30, 32]. In the lowest-order SHM implementation (the P1 method), a single elliptic PDE must be solved. While DOM and variants probably have been used more widely than the others in combustion applications, recent work has shown that SHM methods (P1, P3, etc.) provide a more favorable tradeoff between computational effort and accuracy as one goes to higher-order implementations [34].

PMC/LBL provides a benchmark against which the performance of simpler RTE solvers and/or spectral models can be compared. When combined with the stochastic Lagrangian particle method that is used with the tPDF model for turbulent reacting flows, PMC/LBL has proven to be a powerful approach for computing radiative transfer, including the effects of unresolved turbulent fluctuations in composition and temperature (turbulence-chemistry-soot-radiation interactions) in both Reynolds-averaged [9] and large-eddy simulations [10].

Results are presented for a subset of the available combinations of spectral models and RTE solvers, as described in the following subsection.

3.3. Model combinations considered

Table 3: Summary of model combinations. The benchmark (best) model combination is highlighted using bold font.

Model Designation	Turbulent combustion model	Considers TCI?	RTE solver	Spectral model	Considers emission?	Considers absorption?	Considers TRI?
WSR/noRad	WSR	No	N/A	N/A	N/A	N/A	N/A
WSR/OT/Gray	WSR	No	N/A	Gray	Yes	No	No
WSR/P1/Gray	WSR	No	P1	Gray	Yes	Yes	No
WSR/P1/FSK	WSR	No	P1	FSK	Yes	Yes	No
WSR/PMC/LBL	WSR	No	PMC	LBL	Yes	Yes	No
tPDF/noRad	tPDF	Yes	N/A	N/A	N/A	N/A	N/A
tPDF/OT/Gray/noTRI	tPDF	Yes	N/A	Gray	Yes	No	No
tPDF/OT/Gray/TRI	tPDF	Yes	N/A	Gray	Yes	No	Yes
tPDF/PMC/LBL/noTRI	tPDF	Yes	PMC	LBL	Yes	Yes	No
tPDF/PMC/LBL/TRI	tPDF	Yes	PMC	LBL	Yes	Yes	Yes

In this paper, results for 10 different model combinations are compared (Table 3). These combinations have been chosen to isolate and quantify the various contributors to in-cylinder radiative heat transfer.

The differences between results obtained using WSR versus tPDF models with respect to combustion and emissions (TCI effects) have been discussed in [15]. Here the focus is on radiative heat transfer. To separate TCI effects from TRI effects, tPDF simulations have been performed using particle-level chemistry and radiation (thereby accounting for both TCI and TRI), and with

particle-level chemistry and cell-level radiation (thereby accounting for TCI, while ignoring TRI). Comparisons between results obtained with no radiation model at all (noRad) and those obtained using an optically thin model (OT) that neglects reabsorption provide an overall impression of the potential global importance of radiation. In general, results obtained using a model that considers reabsorption are expected to lie between these two extremes. The importance of spectral radiation properties is determined by comparing results from a gray model that uses Planck-mean absorption coefficients (Gray) with those from a FSK model and from a LBL model. Finally, the influence of the choice of RTE solver is determined by comparing results from PMC with those from a P1 method.

As will be shown in the following section, molecular-gas radiation dominates for all four engine operating conditions. For the tPDF model, the computed end-of-simulation (engine-out) soot levels are in reasonable agreement with experimental measurements, which suggests that the computed in-cylinder soot levels are representative of those in the real engine. To explore situations where soot radiation is more prominent, results are presented for cases where the computed local soot volume fractions are artificially increased by a factor of 100. The factor of 100 is somewhat arbitrary, but is expected to cover the highest levels of soot that would ever be encountered in a practical combustion system. As will be shown below, this corresponds to a scenario where soot radiation is comparable to molecular gas radiation. The soot multiplication is done in a post-processing mode; that is, there is no feedback from the higher soot levels into the CFD simulation. For radiation post-processing, the computed fields have been saved every 2.5 CAD.

4. Results and discussion

The results are organized into two subsections. First, results for the “normal” levels of in-cylinder soot are presented and analyzed in detail. Next, results for the artificially increased high-soot cases are presented. There the emphasis is on differences with respect to the normal soot cases, when broadband soot radiation is relatively more important.

4.1. Normal soot levels

The global influences of radiation on computed in-cylinder pressure traces, heat losses, and pollutant emissions (NO and soot) are discussed first. Subsequent subsections provide insight into the relative importance of the spectral model and RTE solver, soot versus molecular gas radiation, and turbulence-radiation interactions. In the first four subsections, the focus is on part-load and full-load operating conditions with EGR. In the final subsection, differences between EGR and synthetic EGR cases are discussed.

4.1.1. Global radiation effects

Computed and measured in-cylinder pressure traces are compared in Fig. 2 for full-load with EGR operating conditions. Similar results are obtained for the part-load with EGR operating condition, but with a lower peak pressure of approximately 85 bar. Computed results are shown for four different model combinations (Table 3). The influence of TCI can be seen by comparing WSR and tPDF results obtained using the same radiation model. As reported earlier in [15], TCI are important in this engine. The tPDF model, that has been calibrated to be close to the experiment, gives a slower burn rate than the WSR model. On the other hand, the global influence of radiation on combustion is

small. This can be seen in Fig. 2b by comparing results obtained by neglecting radiation altogether (noRad) with those obtained using an optically thin model (OT) for the same turbulent combustion model (WSR or tPDF). The differences in computed peak pressures between noRad and OT are less than 1% for all operating conditions. Results with consideration of reabsorption lie between the noRad and OT results (not shown).

Table 4: End-of-simulation cumulative (from 60° bTDC to 120° aTDC) convective wall heat loss, radiative emission, radiative reabsorption, and radiation reaching walls for two operating conditions with EGR. All values are for the 1/6 sector. The percentages in parentheses are with respect to the corresponding convective wall heat loss.

Operating cond.	Simulations	Wall conv. heat loss (J).	Rad. emiss. (J)	Rad. reabs. (J)	Rad. reaching walls (J)
Part-load EGR	WSR/PMC/LBL	100.54	29.87 (30%)	24.26 (24%)	5.61 (6%)
	tPDF/PMC/LBL/TRI	81.94	27.90 (34%)	22.55 (27%)	5.35 (7%)
Full-load EGR	WSR/PMC/LBL	291.32	143.28 (49%)	126.79 (43%)	16.49 (6%)
	tPDF/PMC/LBL/TRI	232.28	109.10 (47%)	95.70 (41%)	13.40 (6%)

The contributions of radiation to energy redistribution in the combustion chamber and to heat losses are considered next. Figure 3 shows computed cumulative turbulent boundary-layer convective heat loss, total radiative emission over the computational domain, total radiative reabsorption over the computational domain, and radiation reaching the walls (corresponding to a heat loss, for the case of cold black walls) for part-load and full-load with EGR operating conditions. The end-of-simulation values (at 120° aTDC) are summarized in Table 4. For reference, the fuel energy injected (for the 1/6 sector, based on the lower heating value of n-heptane) is approximately 572 J for the part-load and 2068 J for the full-load case. For WSR/PMC/LBL, the convective heat losses

are approximately 18% and 14% of the fuel energy for part-load and full-load with EGR operating conditions, respectively. For tPDF/PMC/LBL/TRI, the convective heat losses are approximately 14% and 11% of the fuel energy for part-load and full-load with EGR operating conditions, respectively. With increasing load, the radiative emission and radiative reabsorption both increase because of the higher pressure; molecular gas radiation dominates over soot radiation, as will be shown later. Total radiative emission is approximately one-third of the convective wall heat loss at part-load, and approximately half of the convective wall heat loss at full-load. Most of the emitted radiation is reabsorbed before reaching a wall (approximately 80% at part load, approximately 90% at full load); radiative transfer redistributes energy within the combustion chamber. For both operating conditions, the radiative energy reaching the walls is approximately 6-7% of the convective wall heat loss.

Local instantaneous mean temperatures in the combustion chamber change by several 10's of Kelvin with consideration of radiative transfer. Figure 4 shows snapshots of computed mean temperature fields at instants close to the time of peak pressure for part-load and full-load with EGR operating conditions. Results are shown for the tPDF model, either neglecting radiation altogether (tPDF/noRad) or using the benchmark radiation model (tPDF/PMC/LBL/TRI). Also shown are the instantaneous fields of the temperature difference between the noRad and the PMC/LBL/TRI radiation models; the differences are as high as 60 K at the instants shown. These local temperature changes alter the local fluid density, and that in turn affects the velocity and turbulent viscosity through the momentum and $k - \epsilon$ equations. They also affect local NO and soot levels, and may result in global changes in computed engine-out pollutant

Table 5: Computed in-cylinder NO and soot at 120° aTDC, and measured engine-out NO and particulate matter. The percentages in parentheses are differences with respect to the corresponding no-radiation case.

	Part-load EGR		Full-load EGR	
	NO (ppm)	Soot (mg)	NO (ppm)	Soot (mg)
Measured	365	5.8e-04	535	1.6e-03
WSR/noRad	318	9.5e-06	521	3.9e-05
WSR/OT/Gray	294 (-7.5%)	9.65e-06 (+1.4%)	470 (-10%)	5.1e-05 (+31%)
WSR/PMC/LBL	310 (-2.5%)	9.1e-06 (-4%)	507 (-2.7%)	3.89e-05 (-0.25%)
tPDF/noRad	181	25.8e-04	312	3.13e-03
tPDF/OT/Gray/TRI	168 (-7.2%)	26.1e-04 (+1.2%)	284 (-9%)	2.93e-03 (-6.3%)
tPDF/PMC/LBL/TRI	178 (-1.7%)	26.1e-04 (+1.2%)	305 (-2.2%)	3.25e-03 (+3.8%)

emissions. That is explored next.

Computed in-cylinder NO and soot are plotted as functions of crank-angle degrees in Figs. 5 and 6, respectively, for part-load and full-load with EGR operating conditions. End-of-simulation (corresponding to engine-out) levels are summarize in Table 5. Results are shown for six model combinations. The pollutant emissions results are more sensitive to the treatment of turbulence-chemistry interactions (differences between WSR and tPDF model results) than they are to the radiation modeling. In particular, the computed NO levels are lower with consideration of TCI (by virtue of the slower combustion and lower temperatures for tPDF compared to WSR) while the computed soot levels are higher with consideration of TCI (for reasons discussed in [15]). Consistent with [15], the tPDF computed soot levels are in better agreement with experimental

measurements. However, in contrast to [15], here the WSR model computed NO levels are in better quantitative agreement with experiment. The computed soot and NO levels are lower than in [15], mainly because of differences in spray modeling. No attempt has been made to reconcile the differences, as here the main focus is on exploring the influence of radiation.

Computed NO levels decrease with consideration of radiation. The largest differences with respect to the no-radiation cases are for the optically thin cases. NO values for cases that consider reabsorption lie between those two extremes, and are closer to the noRad results than to the OT results when a good spectral model (LBL or FSK) is used. Table 5 shows that engine-out NO emissions decrease by 7-10% for OT/Gray and by 1.7-2.7% for PMC/LBL, relative to noRad simulations. The NO results can be understood using a simple thermal argument: higher in-cylinder temperatures result in higher NO. In-cylinder temperatures decrease with consideration of radiative transfer, and the temperature decreases are largest when reabsorption is neglected (OT model). The fraction of emitted radiation that is reabsorbed within the combustion chamber is higher with consideration of spectral radiation properties (FSK or LBL, versus Gray), so that temperatures and NO remain higher when a spectral model is used compared to a gray model.

Engine-out soot is the difference between the total amount of soot that is formed, and the amount of soot that is oxidized before exhaust-valve opening. Differences between WSR and tPDF soot results (the influence of TCI on soot) have been discussed in [15]. The influences of radiative transfer on soot are not as straightforward as the influences on NO, and cannot be explained based

on temperature differences alone. As the temperature decreases, both the production of C_2H_2 (the soot precursor here) and the rate of soot oxidation decrease. Some insight can be gained from an examination of equivalence-ratio-versus-temperature ($\Phi - T$) scatter plots. In Fig. 7, the local equivalence ratio and temperature of each computational element (finite-volume cell for WSR model, notional particle for tPDF method) are plotted at one instant of time for the full-load with EGR operating condition. The boundaries of the zones corresponding to where NO_x and soot formation are expected are also shown [35, 36], where the outer boundaries of the contours are taken from Fig. 2 of [36]. A wider range of thermochemical states is accessed by the tPDF model, especially in the soot zone. For the tPDF/noRAD simulation, approximately 12.4% of the total in-cylinder mass lies within the soot zone at this instant, while for WSR/noRad only 3.4% of the mass is within the soot zone; this explains why the tPDF model produces more soot than the WSR model. The differences in computed mass in the NO_x zone are also consistent with the lower NO_x for tPDF compared to WSR.

The percentages of in-cylinder mass in the NO_x and soot zones for six different model combinations are plotted in Fig. 8 as functions of crank-angle degrees. The NO_x trends are clear, and are consistent with the earlier global temperature-based arguments. On the other hand, the differences in computed soot-zone mass with variations in the radiation model are very small, and any trends are not obvious. Deeper analysis that is beyond the scope of this paper would be needed to unravel the subtle influences of radiative transfer on engine-out soot levels.

Table 6: End-of-simulation cumulative (from 60° bTDC to 120° aTDC) total radiative emission, radiative reabsorption, and radiation reaching walls for two operating conditions. All values are for the 1/6 sector. The percentages in parentheses are differences with respect to the computed reabsorption for PMC/LBL.

Operating cond.	Simulations	Rad. emiss. (J)	Rad. reabs. (J)	Rad. reaching walls (J)
Part-load EGR	WSR/PMC/LBL	29.87	24.26	5.61
	WSR/P1/FSK	29.90	24.24 (0.08%)	5.66
	WSR/P1/Gray	29.28	12.67 (48%)	16.61
	WSR/OT/Gray	28.71	N/A	28.71
Full-load EGR	WSR/PMC/LBL	143.28	126.79	16.49
	WSR/P1/FSK	143.51	126.53 (0.2%)	16.98
	WSR/P1/Gray	141.27	96.56 (24%)	44.71
	WSR/OT/Gray	134.96	N/A	134.96

4.1.2. Influences of spectral model and RTE solver

Computed cumulative total radiative emission, total reabsorption, and radiation reaching walls for part-load and full-load with EGR operating conditions are plotted as functions of crank-angle degrees in Fig. 9 for different combinations of spectral models and RTE solvers, and the end-of-simulation values are tabulated in Table 6. Results from an optically thin model are also given in Table 6. Here WSR model results are shown, as not all combinations of spectral models and RTE solvers are available for the tPDF model. Several observations can be made. First, the total radiative emission and reabsorption are essentially the same for PMC/LBL and for P1/FSK. This suggests two things: that the P1 RTE solver is sufficient for these conditions, and that the FSK spectral model is accurate for these conditions. In general, P1 is expected to perform well for

relatively optically thick systems; that is the case here, as is evident from the high fractions of emitted radiative energy that are reabsorbed before reaching the walls. Second, a gray model significantly underestimates the amount of reabsorption and overestimates the amount of radiative energy that reaches the walls. The differences (with respect to PMC/LBL) in computed reabsorption for P1/Gray are 48% and 24% for the part-load EGR and the full-load EGR cases, respectively. This underprediction of reabsorption results in lower predicted in-cylinder temperatures, which in turn result in slightly lower radiative emission. Finally, when reabsorption is ignored completely (OT model), the computed radiative energy reaching the walls is five-to-eight times higher than the PMC/LBL value. It would be better to ignore radiation altogether than to use an optically thin model.

4.1.3. Soot radiation versus gas radiation

Table 7: Comparisons of end-of-simulation cumulative (from 60° bTDC to 120° aTDC) total radiative emission, radiative reabsorption, and radiation reaching walls for two operating conditions between tPDF/PMC/LBL/TRI and PMC/LBL post-processing of a tPDF/noRad simulation. All values are for the 1/6 sector.

Operating cond.	Simulations	Rad.	Rad.	Rad.
		emiss. (J)	reabs. (J)	reaching walls (J)
Part-load EGR	tPDF/PMC/LBL/TRI	27.90	22.55	5.35
	tPDF/noRad post-processing	28.21	22.78	5.43
Full-load EGR	tPDF/PMC/LBL/TRI	109.10	95.70	13.40
	tPDF/noRad post-processing	110.13	96.59	13.54

Table 8: End-of-simulation cumulative (from 60° bTDC to 120° aTDC) total radiative emission, radiative reabsorption, and radiation reaching walls from three molecular gas species and soot particles for two operating conditions. All values are for the 1/6 sector. The percentages in parentheses are with respect to that species' radiative emission value.

	Part-load EGR			Full-load EGR		
	Rad. emiss. (J)	Rad. reabs. (J)	Rad. reaching walls (J)	Rad. emiss. (J)	Rad. reabs. (J)	Rad. reaching walls (J)
CO ₂	21.45	19.71 (92%)	1.74 (8%)	82.35	78.89 (96%)	3.46 (4%)
H ₂ O	6.19	2.75 (44%)	3.44 (56%)	25.18	15.75 (63%)	9.43 (37%)
CO	0.47	0.31 (66%)	0.17 (34%)	2.32	1.90 (82%)	0.42 (18%)
Soot	0.10	0.01 (10%)	0.09 (90%)	0.28	0.05 (18%)	0.23 (82%)

As shown above, the global influences of radiation on the in-cylinder thermochemical environment are relatively small (less than 10%). Therefore, the contributions of individual molecular gases and soot (which are not saved in the course of the runs with coupled radiation models) can be estimated in a post-processing mode from earlier tPDF/noRad simulations. For this purpose, snapshots saved at 2.5 crank-angle-degrees intervals are analyzed using PMC/LBL at the notional particle level (thereby considering TRI) to compute instantaneous radiative emission and reabsorption fields, with no feedback to the CFD solver. Further justification for the post-processing approach is provided in Table 7, which shows a comparison of total radiative emission, reabsorption, and radiation reaching walls between a coupled tPDF/PMC/LBL/TRI simulation and PMC/LBL post-processing from a tPDF/noRad run. The differences are between 1% and 2%.

Figure 10 shows the cumulative individual contributions of three molecular gas species and soot particles to total radiative emission, reabsorption, and radiation reaching walls as functions of crank-angle degrees for the full-load with EGR operating condition. The end-of-simulation results for two operating conditions are summarized in Table 8. It is evident that radiative emission from CO_2 dominates over other gas species and soot. However, more than 90% of the CO_2 emitted radiative energy is reabsorbed by CO_2 itself and by other molecular gas species and soot, before reaching a wall. On the other hand, just 44% and 63% of the H_2O emitted radiative energy is reabsorbed for part-load and full-load with EGR operating conditions, respectively. Most of the radiative energy emitted by soot particles (~80-90%) reaches the walls, but the net contributions of soot radiation are small – even smaller than those of CO. The radiative energy reaching the walls is dominated by H_2O radiation. Overall, approximately 98% of the radiation reaching walls is from molecular gas radiation, and only 2% is from soot radiation. In Section 4.2 below, results are presented for cases where soot radiation is more prominent.

4.1.4. TRI effects

Instantaneous radiative emission, reabsorption, and radiation reaching walls are plotted as functions of crank-angle degrees in Fig. 11 for tPDF/PMC/LBL/noTRI and tPDF/PMC/LBL/TRI models. Differences between the results from these two models reflect the influence of turbulent fluctuations in composition and temperature on radiative transfer (TRI). Cumulative end-of-simulation results for these two models, and for models that neglect reabsorption (OT), are summarised in Table 9. Emission and reabsorption (the latter for PMC/LBL) both increase with consideration of TRI. The increase in emission is slightly greater

Table 9: Comparisons of end-of-simulation cumulative (from 60° bTDC to 120° aTDC) total radiative emission, radiative reabsorption, and radiation reaching walls between TRI and no-TRI simulations for two operating conditions. All values are for the 1/6 sector. Percentages in parentheses are differences with respect to the corresponding no-TRI case.

Operating cond.	Simulations	Rad. emiss. (J)	Rad. reabs. (J)	Rad. reaching walls (J)
Part-load EGR	tPDF/OT/Gray/noTRI	25.83	N/A	25.83
	tPDF/OT/Gray/TRI	26.44 (2.36%)	N/A	26.44 (2.36%)
	tPDF/PMC/LBL/noTRI	26.79	21.78	5.01
	tPDF/PMC/LBL/TRI	27.90 (4.14%)	22.55 (3.54%)	5.35 (6.8%)
Full-load EGR	tPDF/OT/Gray/noTRI	101.26	N/A	101.26
	tPDF/OT/Gray/TRI	104.15 (2.85%)	N/A	104.15 (2.85%)
	tPDF/PMC/LBL/noTRI	107.12	94.21	12.91
	tPDF/PMC/LBL/TRI	109.10 (1.85%)	95.70 (1.58%)	13.40 (3.8%)

than the increase in absorption, so that the net effect of TRI is a small increase in the radiative energy that reaches the walls. The net effect of TRI on emission can be expressed using following ratios [10, 12]:

$$R_{\text{TRI}} = \frac{\langle \kappa(\mathbf{Y}, T, p) T^4 \rangle}{\kappa(\langle \mathbf{Y} \rangle, \langle T \rangle, p) \langle T \rangle^4} = \underbrace{\frac{\langle \kappa(\mathbf{Y}, T, p) T^4 \rangle}{\langle \kappa(\mathbf{Y}, T, p) \rangle \langle T^4 \rangle}}_{R_{\kappa T^4}} \underbrace{\frac{\langle \kappa(\mathbf{Y}, T, p) \rangle}{\kappa(\langle \mathbf{Y} \rangle, \langle T \rangle, p)}}_{R_{\kappa}} \underbrace{\frac{\langle T^4 \rangle}{\langle T \rangle^4}}_{R_{T^4}} \quad (1)$$

Here, R_{TRI} is the ratio of the cell mean emission that is computed by taking the mean of particle-level emission to the cell emission calculated based on the cell mean temperature and composition fields. It shows the total contributions of temperature and composition fluctuations to radiative emission. This ratio (R_{TRI}) can be decomposed to isolate three individual contributions

of turbulence fluctuations: the absorption coefficient-Planck function correlation ($R_{\kappa T^4}$), the absorption coefficient self-correlation (R_{κ}) and the temperature self-correlation (R_{T^4}).

Figure 12 shows probability density functions of these four ratios at 27.5° aTDC for full-load EGR operating condition. It is evident that most of the $R_{\kappa T^4}$ and R_{κ} values are less than 1.0 (left-side percentages are higher than right-side percentages), while R_{T^4} is always greater than 1.0. The net result is that for 69% of the cells, R_{TRI} is greater than 1.0. As a result, net emission increases with consideration of TRI. The temperature self-correlation term (R_{T^4}) has dominating effect on R_{TRI} . However, the absorption coefficient self-correlation term (R_{κ}) and absorption coefficient-Planck function correlation term ($R_{\kappa T^4}$) cannot be ignored.

Figure 13 and Table 10 show the influence of TRI on computed NO and soot emissions for two operating conditions. With consideration of TRI, engine-out NO emissions decrease by approximately 1%, while engine-out soot decreases by ~3-5% when reabsorption is included.

Table 10: Computed in-cylinder NO and soot at 120° aTDC for two operating conditions. The percentages in parentheses are differences with respect to the corresponding no TRI case.

	Part-load EGR		Full-load EGR	
	NO (ppm)	Soot (mg)	NO (ppm)	Soot (mg)
tPDF/OT/Gray/noTRI	170	24.7e-04	288	3.18e-03
tPDF/OT/Gray/TRI	168 (-1.2%)	26.1e-04 (+5.7%)	284 (-1.4%)	2.93e-03 (-7.8%)
tPDF/PMC/LBL/noTRI	180	27.1e-04	308	3.44e-03
tPDF/PMC/LBL/TRI	178 (-1.1%)	26.1e-04 (-3.7%)	305 (-1%)	3.25e-03 (-5.5%)

The present TRI results are qualitatively consistent with earlier studies of laboratory-scale atmospheric-pressure nonluminous [37–40], luminous (sooting) [9, 10, 41, 42] and pool-fire [43, 44] flames, in that TRI increases both radiative emission and radiative heat loss. However, in contrast to the ~50-100% increase in radiative emission due to TRI in [9], this study shows only a ~2-4% increase in radiative emission due to TRI. Also, here the TRI influence on reabsorption is not negligible compared to the TRI influence on emission, in contrast to the conclusions of [9, 10]. Here, the decrease in NO_x due to TRI is approximately 1%, which is significantly lower compared to the reported values (a factor 2- to -5 times lower) in [40, 42]. Also, recent studies [11, 12] of ECN “Spray A” (liquid n-dodecane fuel) flame concluded that with TRI, radiative emission increases marginally (by less than 10%), and that is consistent with the findings of this paper. The importance of soot on TRI is discussed in Section 4.2.

4.1.5. EGR effects

Table 11: End-of-simulation cumulative (from 60° bTDC to 120° aTDC) convective wall heat loss, radiative emission, radiative reabsorption, and radiation reaching walls for two operating conditions of synthetic EGR. All values are for the 1/6 sector. The percentages in parentheses are with respect to the corresponding convective wall heat loss.

Operating cond.	Simulations	Wall conv.	Rad.	Rad.	Rad. reaching.
		heat loss (J).	emiss. (J)	reabs. (J)	walls (J)
Part-load synthetic EGR	WSR/PMC/LBL	101.22	21.28 (21%)	16.42 (16%)	4.86 (5%)
	tPDF/PMC/LBL/TRI	83.95	20.79 (25%)	16.02 (20%)	4.77 (5%)
Full-load synthetic EGR	WSR/PMC/LBL	293.57	110.50 (38%)	95.19 (33%)	15.31 (5%)
	tPDF/PMC/LBL/TRI	233.88	81.86 (35%)	69.39 (30%)	12.47 (5%)

All results presented up to this point have been for operating conditions with EGR. With EGR, there are radiatively participating molecular gases everywhere in the combustion chamber at all times. Here, the EGR levels considered are approximately 21% EGR by volume. To determine whether or not the EGR has a significant influence on radiation, the synthetic EGR cases are considered (Table 1). For synthetic EGR cases the CO₂ and H₂O in the initial mixture are replaced by N₂, keeping the O₂ concentration and the fuel-oxygen ratio the same as for the corresponding operating condition with EGR. Results are shown in Fig. 14 and Table 11. Comparing Figs. 3 and 14 and Tables 4 and 11, it can be seen that radiative emission and reabsorption for the synthetic EGR operating conditions are both lower (by ~8-10%) compared to those of the corresponding operating condition with EGR. However, the radiative energy reaching the walls remains approximately 5% of the wall boundary layer convective heat loss.

4.2. High soot cases

Table 12: End-of-simulation cumulative (from 60° bTDC to 120° aTDC) convective wall heat loss, radiative emission, radiative reabsorption, and radiation reaching walls for four operating conditions with increased soot. All values are for the 1/6 sector. The percentages in parentheses are with respect to the corresponding convective wall heat loss.

Simulations	Wall conv. heat loss (J).	Rad. emiss. (J)	Rad. reabs. (J)	Rad. reaching walls (J)
Part-load EGR	81.94	38.31 (46%)	28.17 (34%)	10.14 (12%)
Full-load EGR	232.28	137.01 (59%)	114.30 (49%)	22.71 (10%)
Part-load synthetic EGR	83.95	30.96 (37%)	21.43 (26%)	9.53 (11%)
Full-load synthetic EGR	233.88	121.75 (52%)	97.42 (42%)	24.33 (10%)

As shown above, the contributions of soot particles to radiative emission and reabsorption are small compared those of molecular gases for the levels of soot that are present in this engine. The tPDF/noRad computed maximum local (volume-averaged) soot volume fractions for the four operating conditions are: 3.3 ppm (0.14 ppm) for part-load EGR; 8.0 ppm (0.25 ppm) for full-load EGR; 5.2 ppm (0.14 ppm) for part-load synthetic EGR; and 10 ppm (0.33 ppm) for full-load synthetic EGR. To explore a situation where soot radiation is more prominent, here the tPDF/noRad computed soot volume fractions have been multiplied by a factor of 100 for each operating condition, and radiative emission, reabsorption, and radiative energy reaching walls have been computed in a post-processing mode using PMC/LBL. In Table 12, cumulative total radiative emission, reabsorption, and radiation reaching walls for the increased soot cases are tabulated. Comparing Table 12 with Tables 4 and 11, it can be seen that radiative emission and reabsorption both increase with the higher levels of soot, and that the radiative energy reaching walls increases to ~10-12% of the wall convective heat loss. Here it has been assumed that the wall boundary layer convective heat loss remains the same as that for the normal soot condition.

Figure 15 and Table 13 show the contributions of individual molecular gas species and soot particles for the high-soot cases. These can be compared to Fig. 10 and Table 8 for the corresponding normal soot cases. It is evident that even for these very high soot levels, CO₂ emission dominates the radiative emission. But as before, most of the CO₂ emission is reabsorbed before reaching a wall. Now soot is the single largest contributor to radiation reaching the walls, followed closely by H₂O. Approximately 50% of the total radiation reach-

Table 13: End-of-simulation cumulative (from 60° bTDC to 120° aTDC) total radiative emission, radiative reabsorption, and radiation reaching walls from three molecular gas species and soot particles for two operating conditions with increased soot. All values are for the 1/6 sector. The percentages in parentheses are with respect to that species' radiative emission value.

	Part-load EGR			Full-load EGR		
	Rad. emiss. (J)	Rad. reabs. (J)	Rad. reaching walls (J)	Rad. emiss. (J)	Rad. reabs. (J)	Rad. reaching walls (J)
CO ₂	21.42	19.79 (92%)	1.63 (8%)	82.24	78.97 (96%)	3.27 (4%)
H ₂ O	6.17	3.10 (50%)	3.07 (50%)	25.12	16.92 (67%)	8.2 (33%)
CO	0.47	0.33 (70%)	0.14 (30%)	2.31	1.94 (84%)	0.37 (16%)
Soot	10.25	4.95 (48%)	5.30 (52%)	27.34	16.47 (60%)	10.87 (40%)

ing walls is from molecular gas radiation, and approximately 50% is from soot radiation. Hence, in terms of radiation reaching walls, here molecular gas radiation and soot radiation are equally important.

The influence of TRI for the increased soot case is examined in Fig. 16. As seen earlier for the normal soot case, both radiative emission and radiative reabsorption increase with consideration of TRI. Emission increases by 4.8% while reabsorption increases by 5.4%. Figure 16(b) shows the contributions of individual molecular gas species and soot particles, with and without TRI. With consideration of TRI, CO₂ and H₂O cumulative emission increase by approximately 3%, while soot cumulative emission increases by approximately 15%. Figure 17 shows probability density function of four ratio's of Eq. 1. Comparing Fig. 12 and Fig. 17, it can be seen that increased soot increases the absorption coefficient self-correlation term (R_{κ}), such that now 55% of the cells have

R_k values greater than 1.0 (in comparison to 33% of the normal soot case). As a result, 78% (compared to 69% in Fig. 12d) of the cell R_{TRI} values are greater than 1.0, which increase the net TRI effect in comparison to the normal soot condition.

For ECN spray A, Fernandez et al. [11] found that radiative emission from soot increases with consideration of TRI, consistent with the present results. However, in [11] the soot emission approximately doubled with consideration of TRI, while here it increased by just 15%. The difference can be attributed to the difference in rms values of soot volume fraction in the two configurations. A detailed analysis is beyond the scope of this paper.

Finally, computed power spectra of radiative intensities are shown in Fig. 18 for the full-load with EGR operating condition with increased soot. Two spectra are shown: one for the cumulative radiative emission over the full computational domain (Fig. 18a), and the other for the cumulative radiative energy that reaches the walls (Fig. 18b). The broadband spectrum of soot radiative emission is evident, while for gas species two noteworthy bands are dominant: the 4.3 μm band for CO_2 , and the overlapping CO_2 and H_2O bands at 2.7 μm . The spectrum of radiation reaching the walls differs significantly from that of the total emitted radiation, because of reabsorption in (primarily) the CO_2 and H_2O bands. Key differences between the two spectra are: the 4.3 μm CO_2 band is strongly attenuated in the wall spectrum (the system is extremely optically thick at that wavelength); the 2.7 μm $\text{CO}_2/\text{H}_2\text{O}$ overlap band is also strongly attenuated; and the soot spectrum reaching the walls has prominent gaps over these two wavenumber bands, in particular, although the overall attenuation of the soot radiation is small (Table 13). This suggests that a relatively simple

CFD-based model for radiative heat transfer under these conditions might be devised to account for both the spatial redistribution of energy within the cylinder and radiative heat losses to the walls. That is the subject of a recent paper [14].

5. Conclusions

An in-depth investigation of in-cylinder radiative heat transfer has been performed for a heavy-duty diesel truck engine, using URANS-based CFD models. Different engine operating conditions have been considered including part-load and full-load, with and without exhaust-gas recirculation, and different levels of in-cylinder soot. By comparing results obtained using different combinations of turbulent combustion models (well-stirred reactor, and transported probability density function), spectral radiation properties (gray, full-spectrum k -distribution, and line-by-line) and radiative transfer equation solvers (none-optically thin, P1 method, and photon Monte Carlo), the local and global influences of radiation on energy redistribution within the combustion chamber, heat losses, and pollutant emissions have been determined. Based on these findings, a simplified CFD model for radiative transfer in high-pressure combustion systems has been proposed [14]. The major conclusions are as follows.

- Radiative transfer redistributes energy within the combustion chamber, in addition to contributing to heat losses. Total radiative emission is between one-third and one-half of the wall-boundary-layer convective heat loss. However, most of the emitted radiative energy (80-to-90%) is reabsorbed before reaching the walls. For both part-load and full-load operation, and with usual or synthetic EGR, the radiative energy that reaches

the walls is approximately 5-7% of the convective heat loss.

- Molecular gas radiation is more important than soot radiation. Radiative emission from CO₂ dominates the emitted radiation, but the system is optically thick in key CO₂ spectral bands (especially the 4.3 μm band), and most CO₂ radiation is reabsorbed before reaching the walls. A smaller fraction of the radiation emitted by H₂O is reabsorbed, and H₂O radiation dominates the radiative energy that reaches the walls. Most of the broadband soot radiation that is emitted reaches the walls, but the soot contribution is small compared to the molecular gas contributions. For the operating conditions considered here, approximately 98% of the radiative energy reaching the walls is from molecular gases. The soot levels in the engine would need to be approximately 100 times higher for the contribution of soot radiation to be commensurate with that of molecular gas radiation.
- Consideration of spectral radiative properties is essential to accurately predict reabsorption, and consequently, the radiative energy that reaches the walls. A simple gray model gives errors in computed reabsorption of approximately 50% at full-load and 25% at part-load (with EGR). Results from the FSK spectral model are with 1-2% of those from the benchmark LBL model.
- Because molecular gas radiation dominates and the system is relatively optically thick at key spectral bands of CO₂ and H₂O, a simple P1 RTE solver may be sufficient for engine-relevant conditions.
- Local instantaneous mean temperatures in the combustion chamber change

by between 50 and 100 K with consideration of radiation. However, the global effects on computed engine-out NO and soot emissions are small (less than 10%). The influences of radiation on NO are consistent with simple temperature-based arguments. The influences on soot are more subtle and complex, and are not yet fully understood.

- With consideration of TRI, radiative emission and reabsorption both increase by a few percent, and the net effects on radiation reaching walls and pollutant emissions are less than 5%. The largest influence of TRI is an increase in radiative emission from soot particles.
- There are complex spectral interactions that would be difficult, if not impossible, to unravel without PMC/LBL. The CO₂ band at 4.3 μm and the CO₂/H₂O overlap band at 2.7 μm are especially important.
- While the global influences of radiation on wall heat losses and pollutant emissions (NO and soot) are relatively small (between five and ten percent), at the current state of development of engines and of CFD models for in-cylinder processes, it is desirable to explicitly account for radiative heat transfer in CFD simulations. A computationally efficient CFD radiation model that captures the essential aspects of in-cylinder radiation that have been identified here is proposed and demonstrated in [14].
- It is expected that local and global radiation effects will be more prominent in larger, slower, and/or more highly sooting engines: for example, locomotive engines and marine engines. That is the subject of ongoing research.

Acknowledgments

This research has been funded by the U.S. National Science Foundation through grant CBET-1604446. Funding was also provided by the Department of Energy Office of Energy Efficiency and Renewable Energy (EERE) and the Department of Defense, Tank and Automotive Research, Development and Engineering Center (TARDEC), under Award Number DE-EE0007278 .

References

- [1] G. Borman, K. Nishiwaki, Internal-combustion engine heat transfer, *Prog. Energ. Combust.* 13 (1) (1987) 1 – 46.
- [2] M. P. Mengüç, R. Viskanta, C. R. Ferguson, Multidimensional modeling of radiative heat transfer in diesel engines, SAE Technical Paper No. 850503 (1985).
- [3] J. Abraham, V. Magi, Modeling radiant heat loss characteristics in a diesel engine, SAE Technical Paper No. 970888 (1997).
- [4] J. F. Wiedenhofer, R. D. Reitz, A multidimensional radiation model for diesel engine simulation with comparison to experiment, *Numer. Heat Transf. A* 44 (7) (2003) 665–682.
- [5] T. Yoshikawa, R. Reitz, Effect of radiation on diesel engine combustion and heat transfer, *J. Thermal Sci. Technol.* 4 (2009) 86–97.
- [6] J. R. Howell, R. Siegel, M. P. Mengüç, *Thermal Radiation Heat Transfer*, CRC press, 2010.

- [7] W. Yuen, C. Tien, A simple calculation scheme for the luminous-flame emissivity, *Symposium (International) on Combustion* 16 (1) (1977) 1481 – 1487.
- [8] G. Li, M. F. Modest, Numerical simulation of turbulence-radiation interactions in turbulent reacting flows, In *Modelling and Simulation of Turbulent Heat Transfer*, WIT Press, Southampton, England.
- [9] R. S. Mehta, M. F. Modest, D. C. Haworth, Radiation characteristics and turbulence-radiation interactions in sooting turbulent jet flames, *Combust. Theor. Model.* 14 (1) (2010) 105–124.
- [10] A. Gupta, D. Haworth, M. Modest, Turbulence-radiation interactions in large-eddy simulations of luminous and nonluminous nonpremixed flames, *P. Combust. Inst.* 34 (1) (2013) 1281 – 1288.
- [11] S. F. Fernandez, C. Paul, A. Sircar, A. Imren, D. Haworth, S. Roy, M. Modest, Soot and spectral radiation modeling for high-pressure turbulent spray flames, *Combust. Flame* 190 (2018) 402 – 415.
- [12] M. Bolla, M. A. Chishty, E. R. Hawkes, Q. N. Chan, S. Kook, Influence of turbulent fluctuations on radiation heat transfer, soot and soot formation under ecn spray a conditions, *P. Combust. Inst.* 36 (3) (2017) 3551 – 3558.
- [13] P. Coelho, Numerical simulation of the interaction between turbulence and radiation in reactive flows, *Prog. Energ. Combust.* 33 (2007) 311–383.
- [14] C. Paul, D. C. Haworth, M. F. Modest, A simplified CFD model for spectral radiative heat transfer in high-pressure

- hydrocarbon-air combustion systems, *P. Combust. Inst.* 36 (2019).
doi:<https://doi.org/10.1016/j.proci.2018.08.024>.
- [15] V. R. Mohan, D. Haworth, Turbulence-chemistry interactions in a heavy-duty compression-ignition engine, *P. Combust. Inst.* 35 (3) (2015) 3053 – 3060.
- [16] Openfoam.
URL <https://openfoam.org/>
- [17] S. E. Tahry, k-epsilon equation for compressible reciprocating engine flows turbulent flow and heat transfer, *J. Energy* 7 (4) (1983) 345–353.
- [18] C. Angelberger, T. Poinso, B. Delhay, Improving near-wall combustion and wall heat transfer modeling in si engine computations, SAE Technical Paper No. 972881.
- [19] V. I. Golovitchev, Chalmers University of Technology, Gothenburg, Sweden (2000).
URL <http://www.tfd.chalmers.se/%7EValeri/MECH.html>
- [20] K. Leung, R. Lindstedt, W. Jones, A simplified reaction mechanism for soot formation in nonpremixed flames, *Combust. Flame* 87 (3) (1991) 289 – 305.
- [21] H. Guo, F. Liu, G. J. Smallwood, Soot and NO formation in counterflow ethylene/oxygen/nitrogen diffusion flames, *Combust. Theor. Model.* 8 (3) (2004) 475–489.
- [22] S. Pope, PDF methods for turbulent reactive flows, *Prog. Energ. Combust.* 11 (2) (1985) 119 – 192.

- [23] D. Haworth, Progress in probability density function methods for turbulent reacting flows, *Prog. Energ. Combust.* 36 (2) (2010) 168 – 259.
- [24] S. Subramaniam, S. Pope, A mixing model for turbulent reactive flows based on Euclidean minimum spanning trees, *Combust. Flame* 115 (4) (1998) 487 – 514.
- [25] J. K. Dukowicz, A particle-fluid numerical model for liquid sprays, *J. Comput. Phys.* 35 (2) (1980) 229 – 253.
- [26] Z. Han, S. Parrish, P. V. Farrell, R. D. Reitz, Modeling atomization processes of pressure-swirl hollow-cone fuel sprays, *Atomization Spray* 7 (6) (1997) 663–684.
- [27] A. H. Lefebvre, V. G. McDonell, *Atomization Spray*, 2nd Edition, CRC Press, Taylor and Francis, 2017.
- [28] R. Reitz, R. Diwaker, Effect of drop breakup on fuel sprays, SAE Technical Paper No. 860469.
- [29] R. Reitz, Modeling atomization processes in high-pressure vaporizing sprays, *Atomisation Spray Technology* 3 (1987) 309–337.
- [30] M. F. Modest, D. C. Haworth, *Radiative Heat Transfer in Turbulent Combustion Systems*, Springer, 2016.
- [31] L. Rothman, I. Gordon, R. Barber, H. Dothe, R. Gamache, A. Goldman, V. Perevalov, S. Tashkun, J. Tennyson, HITEMP, the high-temperature molecular spectroscopic database, *J. Quant. Spectrosc. Ra.* 111 (15) (2010) 2139 – 2150.

- [32] M. F. Modest, Radiative Heat Transfer, 3rd Edition, Academic Press, Boston, 2013.
- [33] H. Chang, T. T. Charalampopoulos, Determination of the wavelength dependence of refractive indices of flame soot, Proceedings of the Royal Society of London A: Mathematical, Physical and Engineering Sciences 430 (1880) (1990) 577–591.
- [34] G. Pal, A. Gupta, M. F. Modest, D. C. Haworth, Comparison of accuracy and computational expense of radiation models in simulation of non-premixed turbulent jet flames, Combust. Flame 162 (6) (2015) 2487 – 2495.
- [35] S. Kook, C. Bae, P. C. Miles, D. Choi, L. M. Pickett, The influence of charge dilution and injection timing on low-temperature diesel combustion and emissions, SAE Technical Paper No. 2005-01-3837.
- [36] J. E. Dec, Advanced compression-ignition engines – understanding the in-cylinder processes, P. Combust. Inst. 32 (2) (2009) 2727 – 2742.
- [37] G. Li, M. F. Modest, Application of composition pdf methods in the investigation of turbulence-radiation interactions, J. Quant. Spectrosc. Ra. 73 (2) (2002) 461 – 472.
- [38] J. Frank, R. Barlow, C. Lundquist, Radiation and nitric oxide formation in turbulent non-premixed jet flames, P. Combust. Inst. 28 (1) (2000) 447 – 454.
- [39] P. Coelho, Detailed numerical simulation of radiative transfer in a nonluminous turbulent jet diffusion flame, Combust. Flame 136 (4) (2004) 481 – 492.

- [40] A. Habibi, B. Merci, D. Roekaerts, Turbulence radiation interaction in Reynolds-averaged Navier-Stokes simulations of nonpremixed piloted turbulent laboratory-scale flames, *Combust. Flame* 151 (1) (2007) 303 – 320.
- [41] L. Tessé, F. Dupoirieux, J. Taine, Monte Carlo modeling of radiative transfer in a turbulent sooty flame, *Int. J. Heat Mass Tran.* 47 (3) (2004) 555 – 572.
- [42] L. Wang, D. Haworth, S. Turns, M. Modest, Interactions among soot, thermal radiation, and nox emissions in oxygen-enriched turbulent non-premixed flames: A computational fluid dynamics modeling study, *Combust. Flame* 141 (1) (2005) 170 – 179.
- [43] J. Consalvi, Influence of turbulence-radiation interactions in laboratory-scale methane pool fires, *Int. J. Therm. Sci.* 60 (2012) 122 – 130.
- [44] J. Consalvi, R. Demarco, A. Fuentes, S. Melis, J. Vantelon, On the modeling of radiative heat transfer in laboratory-scale pool fires, *Fire Safety J.* 60 (2013) 73 – 81.

List of Figures

1	Engine sector meshes at 30° aTDC. (a) 51,225-cell mesh used from 30° bTDC to 30° aTDC. (b) 85,650-cell mesh used from 60° bTDC to 30° bTDC, and from 30° aTDC to 120° aTDC.	44
2	Computed and measured in-cylinder pressure traces for full-load with EGR operating conditions. (a) full simulation (b) zoomed in around the peak pressure.	44
3	Computed cumulative boundary-layer convective wall heat loss, total radiative emission, total radiative reabsorption, and radiation reaching walls (or radiative heat loss) for two operating conditions of tPDF/PMC/LBL/TRI simulation as functions of crank-angle degrees. (a) Part-load with EGR. (b) Full-load with EGR. . . .	45
4	Computed (tPDF model) instantaneous mean temperature contours on a cutting plane containing the injection axis. Results obtained neglecting radiation (tPDF/noRad) are compared with those obtained using the benchmark radiation model (tPDF/PMC/LBL/TRI). Also plotted is the difference in the computed temperature fields between the two models. Part-load results are plotted at 10° aTDC, and full-load results are plotted at 15° aTDC.	46
5	Computed in-cylinder NO as a function of crank-angle degrees for six model combinations and two operating conditions. (a) Part-load with EGR. (b) Full-load with EGR.	46
6	Computed in-cylinder soot as a function of crank-angle degrees for six model combinations and two operating conditions. (a) Part-load with EGR. (b) Full-load with EGR.	47

7	Computed scatter plots of equivalence ratio versus temperature for the full-load with EGR operating condition at 15° aTDC. The percentages are the percent of total in-cylinder mass that falls within the “soot zone” and the “NOx zone.” (a) WSR/noRad model. (b) tPDF/noRad model.	47
8	Percentages of total in-cylinder mass that lie within the NOx and soot zones as functions of crank-angle degrees for six model combinations, for the full-load with EGR operating condition. (a) NOx zone. (b) Soot zone.	48
9	Cumulative radiative emission, reabsorption, and radiation reaching walls as functions of crank-angle degrees for three model combinations. (a) Part-load with EGR. (b) Full-load with EGR.	48
10	Cumulative radiative emission, reabsorption, and radiation reaching walls from three molecular gas species and soot particles as functions of crank-angle degrees for the full-load with EGR operating condition. Here the individual reabsorption curves show the amount of radiative energy emitted by that species that is reabsorbed by all molecular gas species and by soot. (a) Radiative emission and reabsorption. (b) Radiation reaching walls.	49
11	Computed instantaneous total radiative emission, reabsorption, and radiation reaching walls as functions of crank-angle degrees for tPDF/PMC/LBL/noTRI and tPDF/PMC/LBL/TRI, for two operating conditions. (a) Part-load with EGR. (b) Full-load with EGR.	49

12	Probability density function of R_{KT^4} , R_K , R_{T^4} and R_{TRI} , as shown in Eq. 1, at 27.5° aTDC for full-load EGR operating condition. A vertical blue line is shown at $R = 1$ for demarcation. The percentages at the left and right of the blue line denotes percentage of cells for which the corresponding ratio is less than or greater than 1.0, respectively.	50
13	Computed instantaneous in-cylinder NO and soot as functions of crank-angle degrees for the full-load with EGR operating condition, with versus without consideration of TRI. (a) NO. (b) Soot.	51
14	Computed cumulative boundary-layer convective wall heat loss, total radiative emission, total radiative reabsorption, and radiation reaching walls (or radiative heat loss) as functions of crank-angle degrees for two operating conditions of synthetic EGR. (a) Part-load synthetic EGR. (b) Full-load synthetic EGR.	51
15	Cumulative radiative emission, reabsorption, and radiation reaching walls from three molecular gas species and soot particles as functions of crank-angle degrees for the full-load with EGR operating condition with increased soot. Here the individual reabsorption curves show the amount of radiative energy emitted by that species that is reabsorbed by all molecular gas species and by soot. (a) Radiative emission and reabsorption. (b) Radiation reaching walls.	52

16	Computed instantaneous total radiative emission, reabsorption, and radiation reaching walls as functions of crank-angle degrees for PMC/LBL post-processing of the tPDF/noRad full-load with EGR operating condition with increased soot, with versus without consideration of TRI. (a) Totals. (b) Contributions of individual molecular gas species and soot particles.	52
17	Probability density function of R_{kT^4} , R_k , R_{T^4} and R_{TRI} , as shown in Eq. 1, at 27.5° aTDC for increased soot case of full-load EGR operating condition. A vertical blue line is shown at $R = 1$ for demarcation. The percentages at the left and right of the blue line denotes percentage of cells for which the corresponding ratio is less than or greater than 1.0, respectively.	53
18	Computed cumulative power spectra over the computed engine cycle of radiative intensity for the increased soot full-load with EGR operating condition. a) Spectrum of radiation emitted over the full computational domain. b) Spectrum of radiation reaching walls.	54

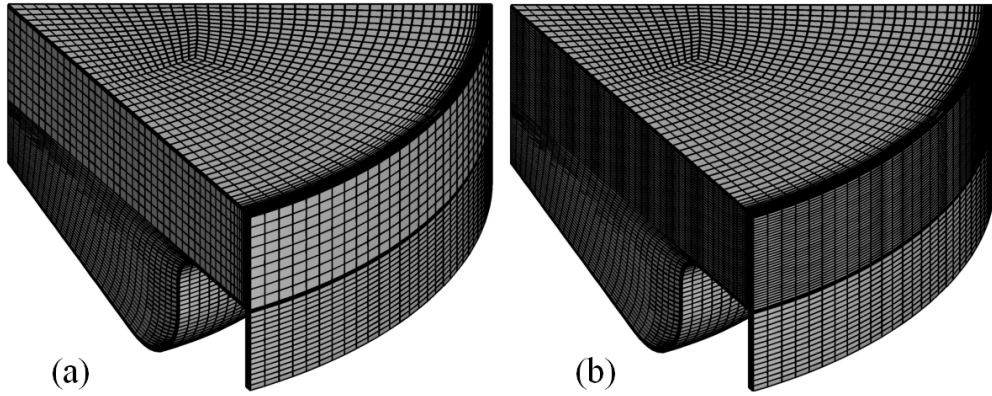


Figure 1: Engine sector meshes at 30° aTDC. (a) 51,225-cell mesh used from 30° bTDC to 30° aTDC. (b) 85,650-cell mesh used from 60° bTDC to 30° bTDC, and from 30° aTDC to 120° aTDC.

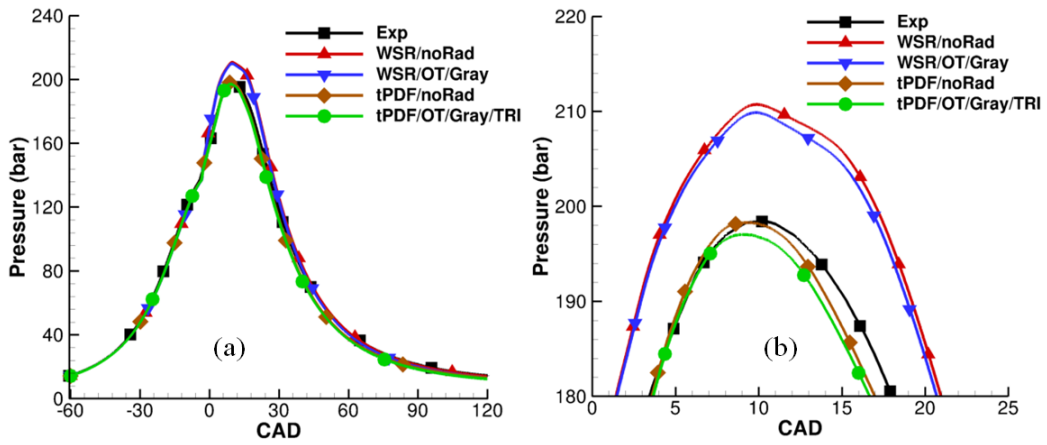


Figure 2: Computed and measured in-cylinder pressure traces for full-load with EGR operating conditions. (a) full simulation (b) zoomed in around the peak pressure.

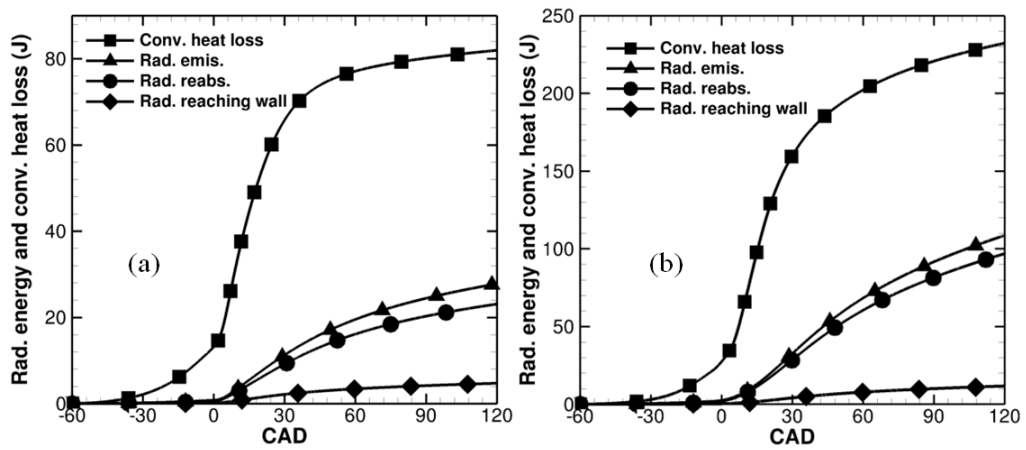


Figure 3: Computed cumulative boundary-layer convective wall heat loss, total radiative emission, total radiative reabsorption, and radiation reaching walls (or radiative heat loss) for two operating conditions of tPDF/PMC/LBL/TRI simulation as functions of crank-angle degrees. (a) Part-load with EGR. (b) Full-load with EGR.

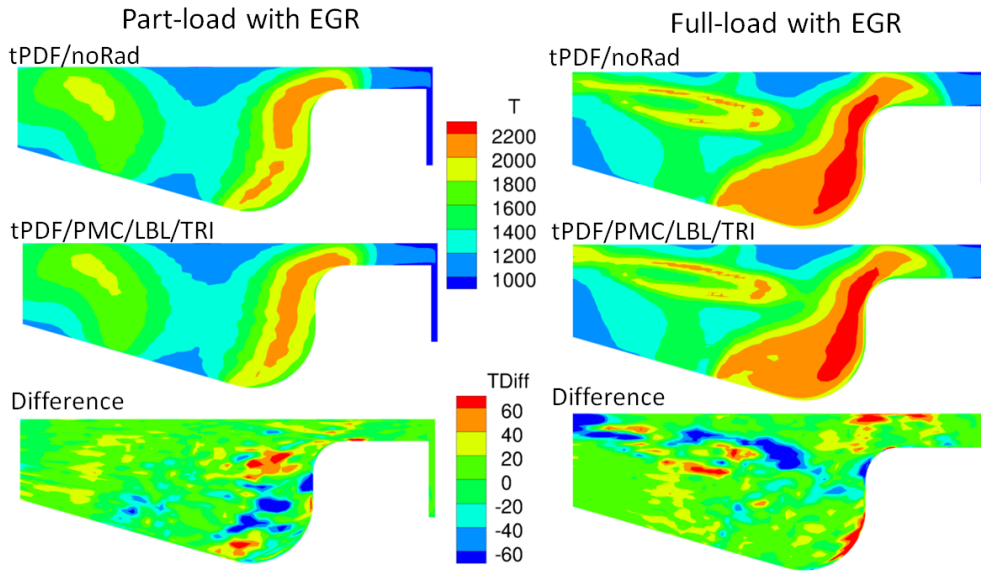


Figure 4: Computed (tPDF model) instantaneous mean temperature contours on a cutting plane containing the injection axis. Results obtained neglecting radiation (tPDF/noRad) are compared with those obtained using the benchmark radiation model (tPDF/PMC/LBL/TRI). Also plotted is the difference in the computed temperature fields between the two models. Part-load results are plotted at 10° aTDC, and full-load results are plotted at 15° aTDC.

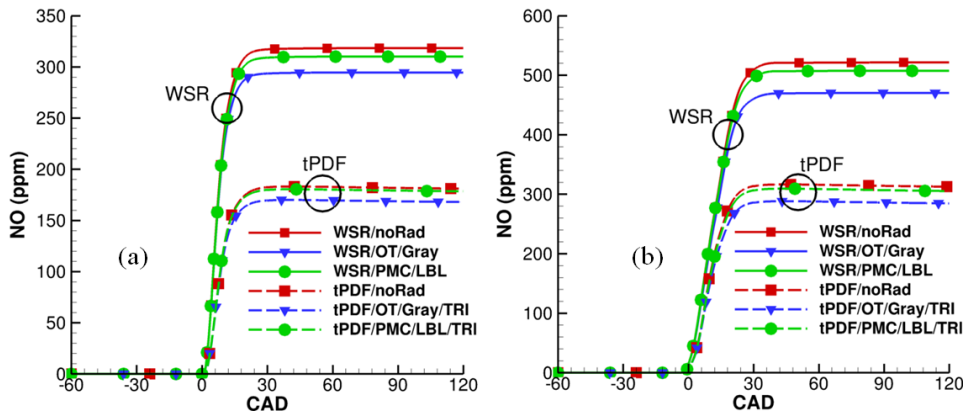


Figure 5: Computed in-cylinder NO as a function of crank-angle degrees for six model combinations and two operating conditions. (a) Part-load with EGR. (b) Full-load with EGR.

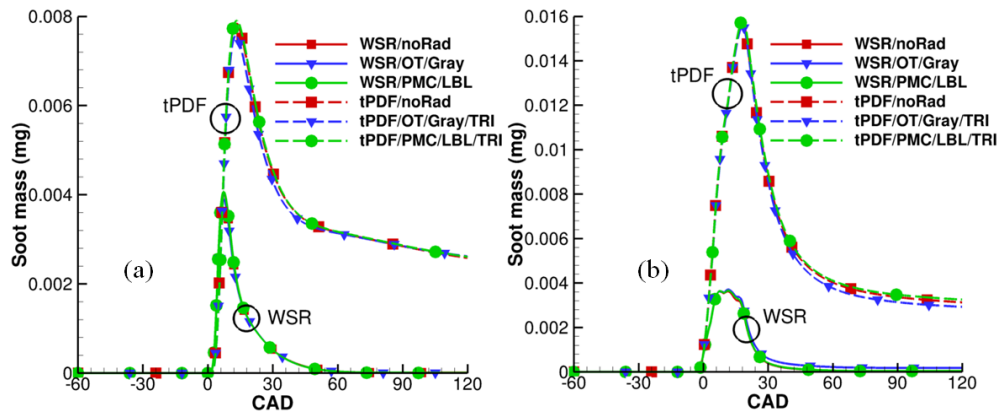


Figure 6: Computed in-cylinder soot as a function of crank-angle degrees for six model combinations and two operating conditions. (a) Part-load with EGR. (b) Full-load with EGR.

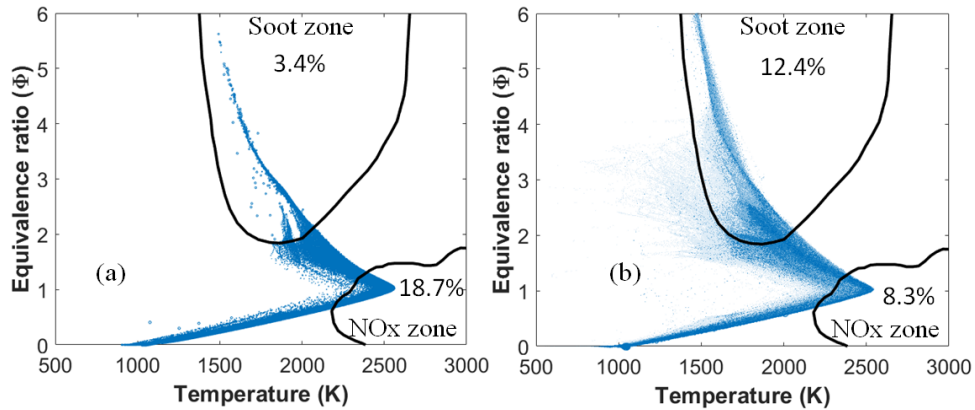


Figure 7: Computed scatter plots of equivalence ratio versus temperature for the full-load with EGR operating condition at 15° aTDC. The percentages are the percent of total in-cylinder mass that falls within the “soot zone” and the “NOx zone.” (a) WSR/noRad model. (b) tPDF/noRad model.

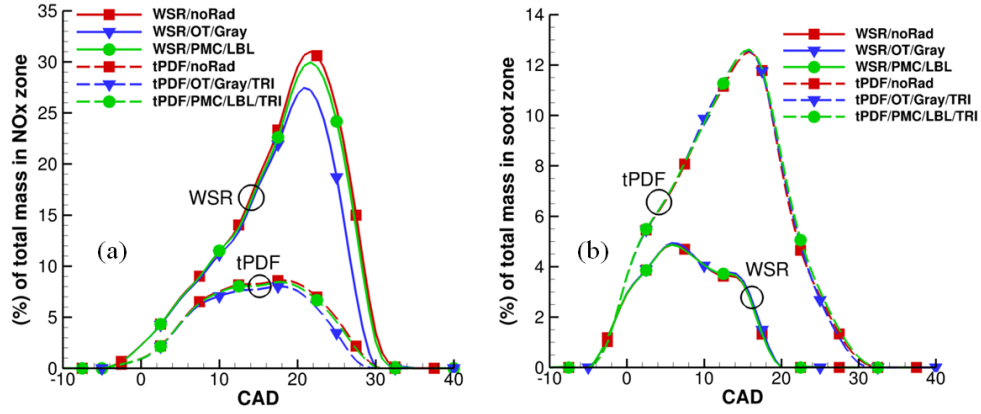


Figure 8: Percentages of total in-cylinder mass that lie within the NOx and soot zones as functions of crank-angle degrees for six model combinations, for the full-load with EGR operating condition. (a) NOx zone. (b) Soot zone.

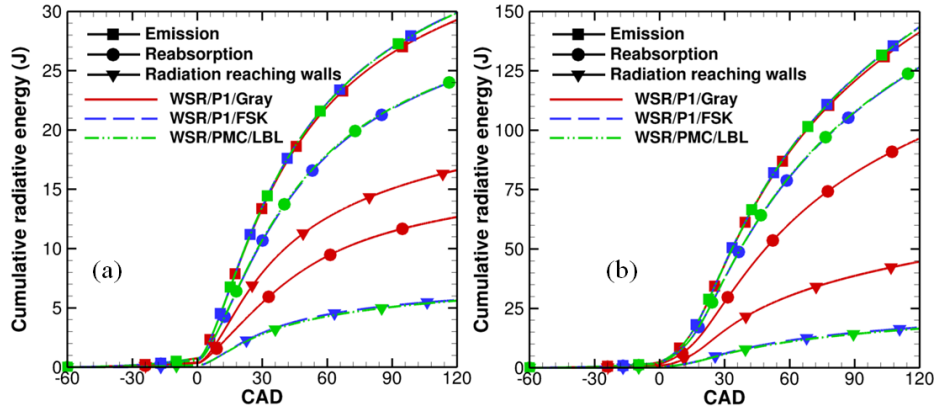


Figure 9: Cumulative radiative emission, reabsorption, and radiation reaching walls as functions of crank-angle degrees for three model combinations. (a) Part-load with EGR. (b) Full-load with EGR.

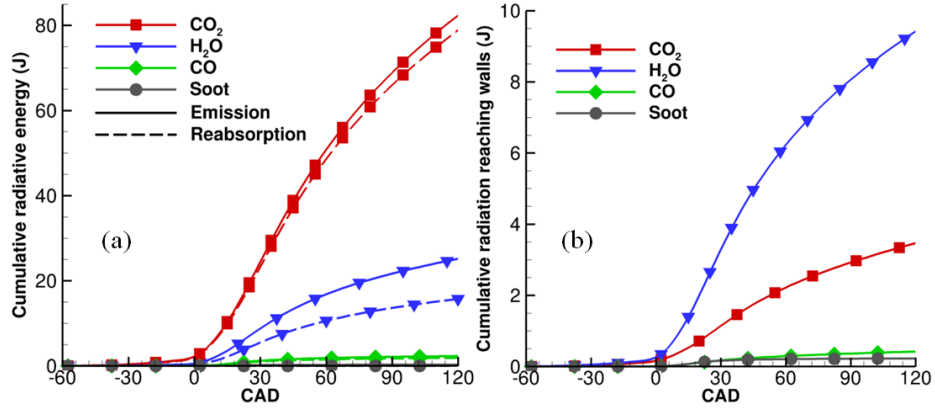


Figure 10: Cumulative radiative emission, reabsorption, and radiation reaching walls from three molecular gas species and soot particles as functions of crank-angle degrees for the full-load with EGR operating condition. Here the individual reabsorption curves show the amount of radiative energy emitted by that species that is reabsorbed by all molecular gas species and by soot. (a) Radiative emission and reabsorption. (b) Radiation reaching walls.

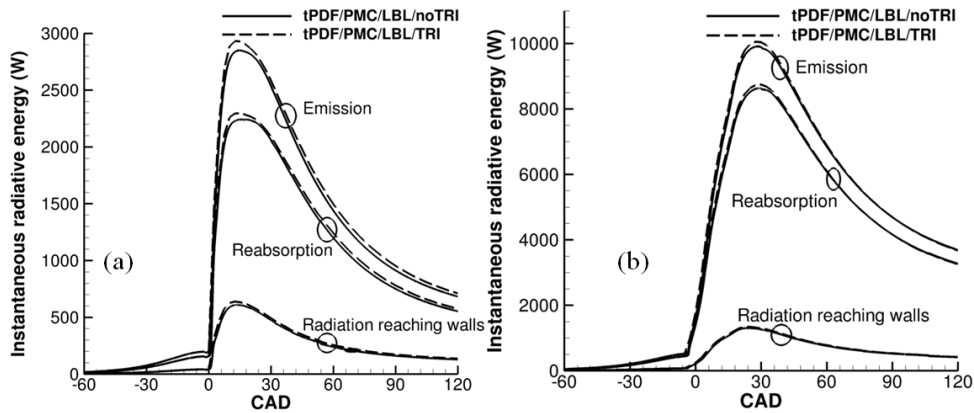


Figure 11: Computed instantaneous total radiative emission, reabsorption, and radiation reaching walls as functions of crank-angle degrees for tPDF/PMC/LBL/noTRI and tPDF/PMC/LBL/TRI, for two operating conditions. (a) Part-load with EGR. (b) Full-load with EGR.

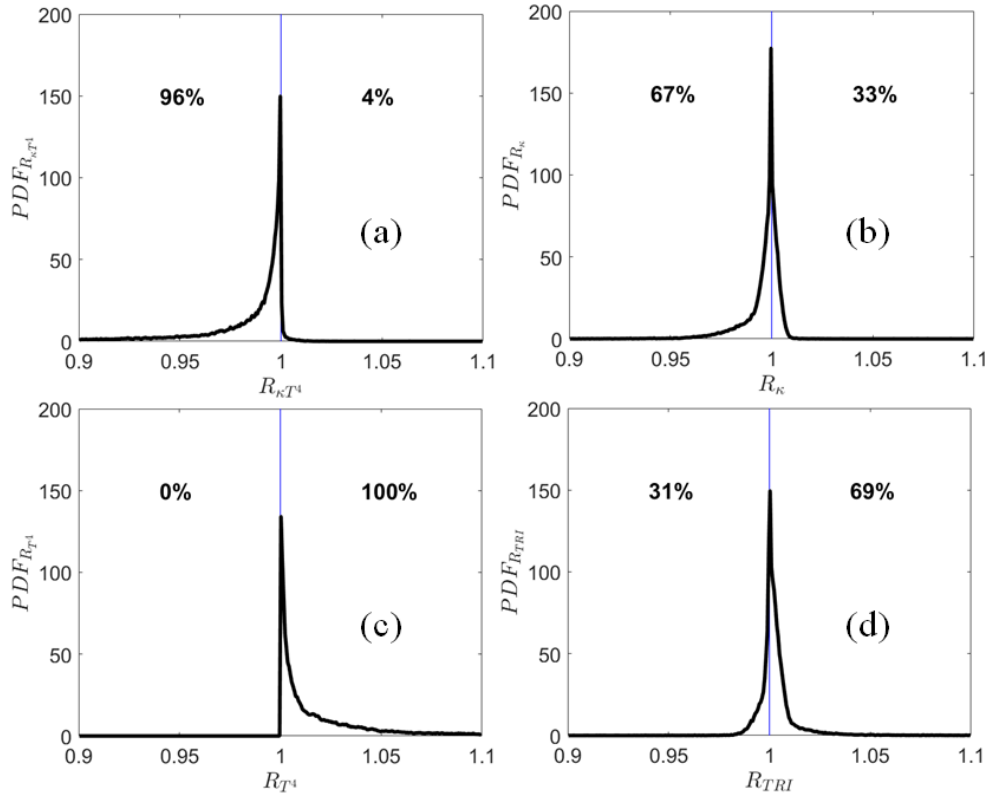


Figure 12: Probability density function of R_{kT^4} , R_k , R_{T^4} and R_{TRI} , as shown in Eq. 1, at 27.5° aTDC for full-load EGR operating condition. A vertical blue line is shown at $R = 1$ for demarcation. The percentages at the left and right of the blue line denotes percentage of cells for which the corresponding ratio is less than or greater than 1.0, respectively.

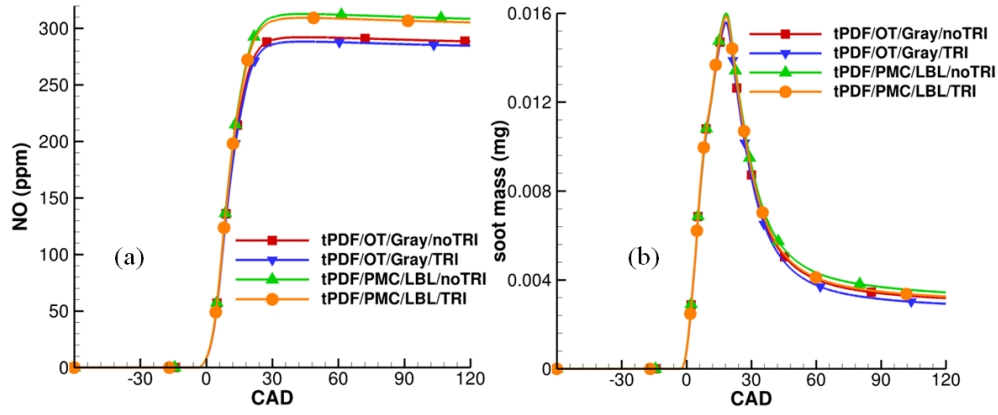


Figure 13: Computed instantaneous in-cylinder NO and soot as functions of crank-angle degrees for the full-load with EGR operating condition, with versus without consideration of TRI. (a) NO. (b) Soot.

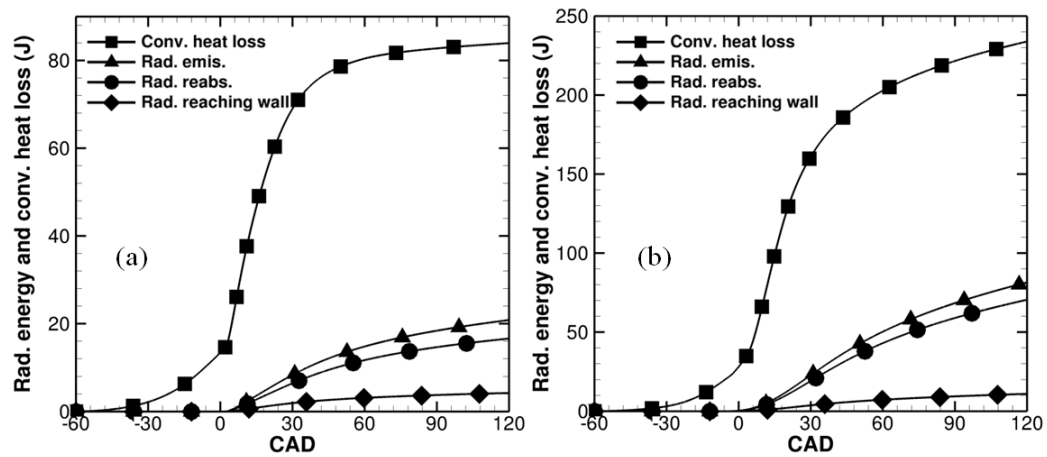


Figure 14: Computed cumulative boundary-layer convective wall heat loss, total radiative emission, total radiative reabsorption, and radiation reaching walls (or radiative heat loss) as functions of crank-angle degrees for two operating conditions of synthetic EGR. (a) Part-load synthetic EGR. (b) Full-load synthetic EGR.

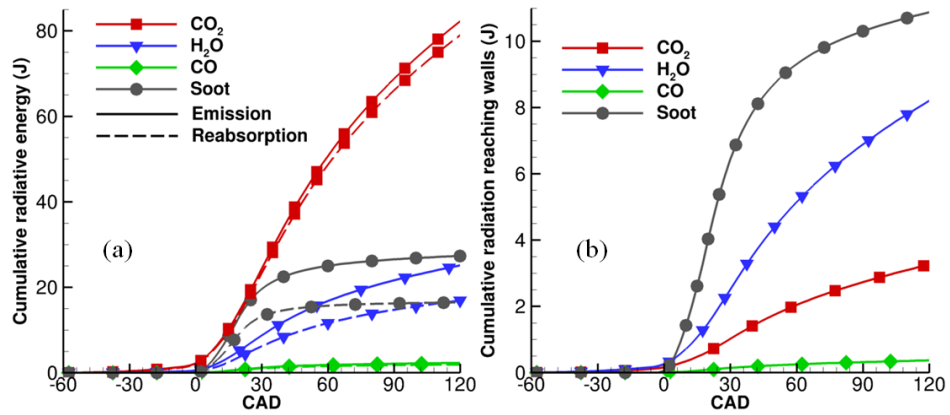


Figure 15: Cumulative radiative emission, reabsorption, and radiation reaching walls from three molecular gas species and soot particles as functions of crank-angle degrees for the full-load with EGR operating condition with increased soot. Here the individual reabsorption curves show the amount of radiative energy emitted by that species that is reabsorbed by all molecular gas species and by soot. (a) Radiative emission and reabsorption. (b) Radiation reaching walls.

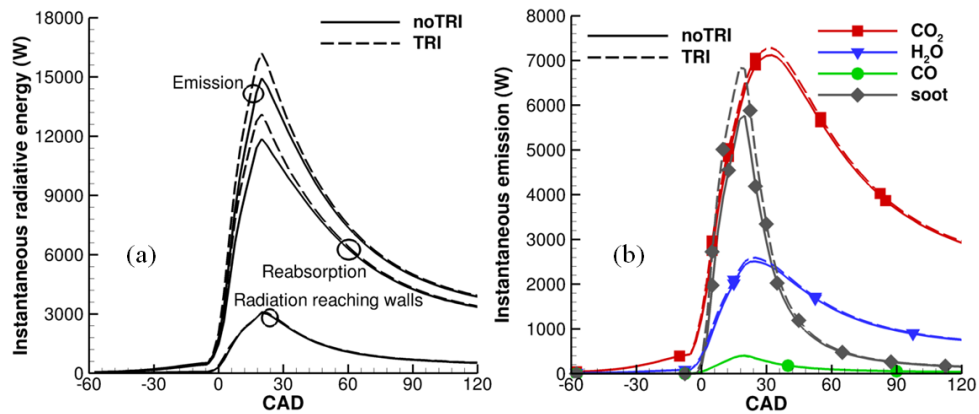


Figure 16: Computed instantaneous total radiative emission, reabsorption, and radiation reaching walls as functions of crank-angle degrees for PMC/LBL post-processing of the tPDF/noRad full-load with EGR operating condition with increased soot, with versus without consideration of TRI. (a) Totals. (b) Contributions of individual molecular gas species and soot particles.

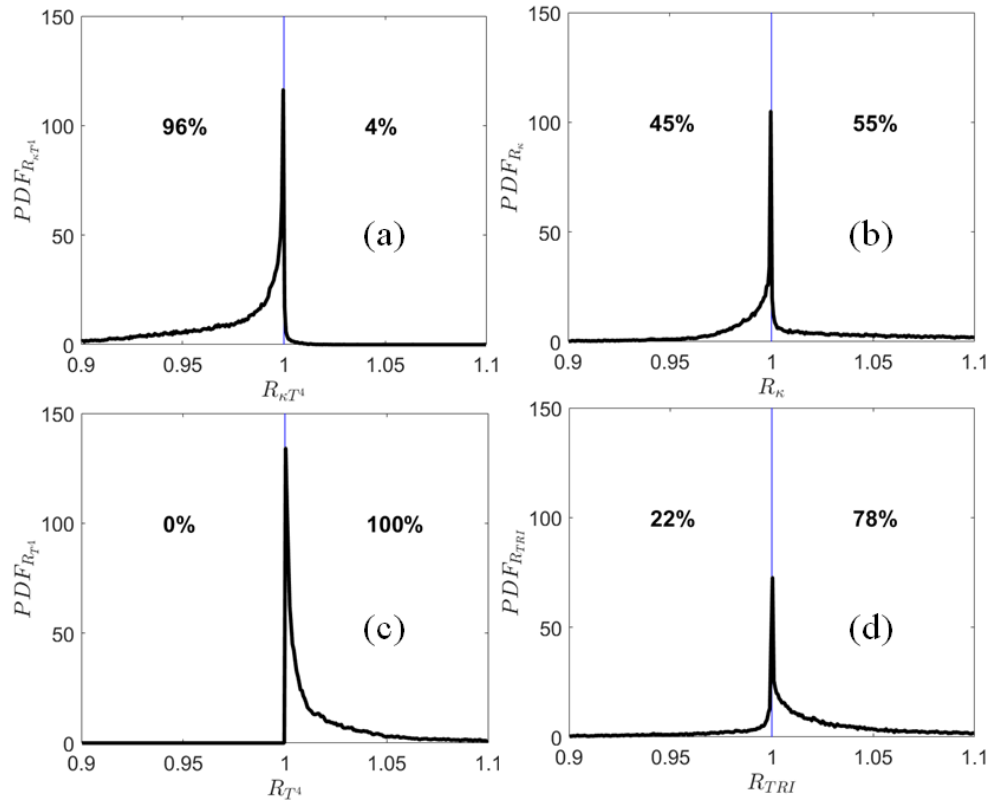


Figure 17: Probability density function of R_{kT^4} , R_k , R_{T^4} and R_{TRI} , as shown in Eq. 1, at 27.5° aTDC for increased soot case of full-load EGR operating condition. A vertical blue line is shown at $R = 1$ for demarcation. The percentages at the left and right of the blue line denotes percentage of cells for which the corresponding ratio is less than or greater than 1.0, respectively.

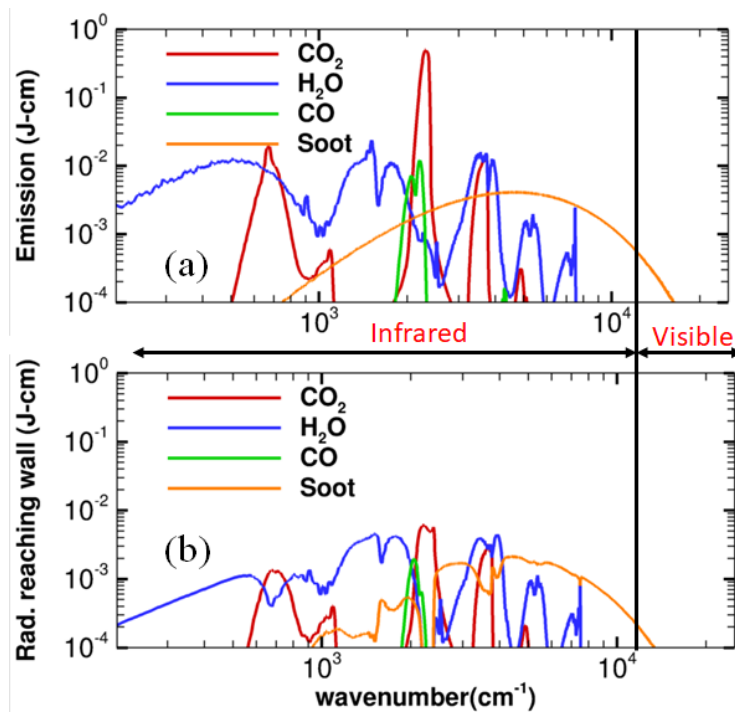


Figure 18: Computed cumulative power spectra over the computed engine cycle of radiative intensity for the increased soot full-load with EGR operating condition. a) Spectrum of radiation emitted over the full computational domain. b) Spectrum of radiation reaching walls.